ROYAL SOCIETY
OF CHEMISTRY

PAPER

Elucidating the reversible exsolution–dissolution behaviour of high-entropy oxides in crystalline and amorphous phases

Qingju Wang,†[a] Hailing Yu, ID †[a] Kevin Siniard,[a] Zhenzhen Yang[b] and Sheng Dai ID *[ab]

High-entropy oxides (HEOs), as a subclass of high-entropy materials (HEMs), offer a versatile platform for catalysis by leveraging entropy-stabilized solid solutions with tunable compositions, lattice structures, and electronic properties. While exsolution–dissolution of metal species in crystalline HEOs has emerged as a promising strategy for reversible active sites regeneration, the dynamic behaviour of HEOs possessing amorphous nature remains under-explored, particularly the difference with crystalline counterparts. In this work, we systematically investigate the architecture-dependent exsolution–dissolution behavior of HEOs by comparing a crystalline-phase HEO (c-HEO) and an amorphous-phase HEO (a-HEO), both comprising Ni, Mg, Cu, Zn, and Co as principal metal elements. Using a combination of *in situ* variable-temperature X-ray diffraction (XRD), X-ray photoelectron spectroscopy (XPS), electron microscopy, and *in situ* CO diffuse reflectance infrared Fourier transform spectroscopy (CO-DRIFTS), the structural evolution of the two HEO phases under redox conditions was elucidated. Both materials exhibit reversible exsolution of metallic species or alloys in reducing environments, followed by re-incorporation into the host lattice upon oxidation. Remarkably, the a-HEO demonstrates more facile and dynamic self-healing behavior, with alloy exsolution and dissolution occurring under milder conditions because of its enhanced reducibility and structural disorder. This study provides critical insights into the design of next-generation regenerable catalysts based on amorphous HEOs, highlighting the role of phase structure in governing reversible metal-site formation dynamics and catalytic performance.

1 Introduction

High-Entropy Materials (HEMs) have emerged as a versatile platform for addressing persistent challenges in catalysis that remain unsolved by traditional,

[a]Department of Chemistry, University of Tennessee Knoxville, Knoxville, TN 37996, USA
[b]Chemical Sciences Division, Oak Ridge National Laboratory, Oak Ridge, TN 37831, USA. E-mail: dais@ornl.gov
† Q. Wang and H. Yu contributed equally to this work.

enthalpy-dominated systems.[1–3] A wide spectrum of HEMs has been developed, incorporating metallic or cationic elements into solid solutions such as entropy-stabilized alloys, oxides, nitrides, carbides, fluorides, sulfides, phosphides, and inorganic–organic hybrids. These materials have demonstrated promising performance across diverse catalytic applications, including thermocatalysis, electrocatalysis, and photocatalysis.[2,4–10] HEMs are formed by incorporating multiple principal elements into a single crystalline lattice, stabilized primarily by high configurational entropy.[10–15] This entropy-driven stabilization often results in well-defined crystal structures, where the synergistic effects of lattice distortion and chemical disorder give rise to unique catalytic properties. These include exceptional thermal and structural stability under harsh reaction conditions, as well as a high density of tunable defects that can modulate the electronic environment of active sites within the host lattice.[16,17]

High-entropy oxides (HEOs) are among the most extensively studied subclasses of HEMs, distinguished by their independently tunable cation and anion sublattices, which enable exceptional flexibility in both structure and composition.[18–21] Since the first report of a rock salt-structured (NiMgCuZnCo)O_x in 2015,[22] HEOs have rapidly gained attention for their catalytic potential, with their first application in oxidative catalysis demonstrated in 2018.[23] A wide range of crystal structures, including rock salt, fluorite, perovskite, and spinel, has since been explored, positioning HEOs as both active catalysts and supports across diverse catalytic processes.[1,24–31] Their structural diversity and chemical complexity allow for applications in thermal catalysis (*e.g.*, alcohol oxidation, CO oxidation, methane combustion, CO_2 hydrogenation, and dry reforming of methane) and electrocatalysis (*e.g.*, water splitting, the hydrogen evolution reaction, and the oxygen evolution reaction). A key advantage of HEOs lies in their ability to accommodate multiple aliovalent cations within a single-phase lattice, enabling flexible tuning of local coordination environments and electronic structures, which facilitates the generation of oxygen vacancies and enhances activity in oxidative reactions such as aerobic alcohol oxidation,[32] oxidative desulfurization,[33] and CO oxidation.[23,34–38] Moreover, this structural tunability makes HEOs ideal platforms for anchoring and stabilizing noble metal species at the atomic scale. For instance, Pt single atoms embedded within the rock salt lattice of (NiMgCuZnCo)O_x have demonstrated excellent activity and durability for CO oxidation,[23] while Pd single atoms stabilized in a fluorite-structured CeZrHfTiLaO_x matrix showed high performance in the oxidative conversion of gas mixtures containing CO, propene, and NO.[39]

In addition to their direct use in oxidation reactions, HEO and HEO-stabilized noble metal catalysts offer promising platforms for stabilizing reduced metal nanoparticles (NPs) and single atoms (SAs), benefiting their entropy-driven stability, structural diversity, and tunability in metal composition and lattice structure.[1,40] Notably, the self-regenerative exsolution–dissolution behavior of HEOs enables the development of highly efficient and durable catalysts for reduction reactions.[41] For example, the temperature-dependent exsolution behavior of Au NPs in rock salt-structured NiMgCuZnCoO$_x$ was revealed through a thermally induced phase transition.[42] Contrary to conventional sintering behavior of metal catalysts, where elevated temperatures promote particle aggregation, Au species in the Au-HEO catalyst, synthesized *via* mechanochemical

treatment and calcination at 900 °C in air, were fully integrated into the HEO lattice, as indicated by the absence of Au signals and lattice expansion in the XRD pattern of Au-HEO. Interestingly, when calcined at 700 °C, exsolution of Au was observed due to reduced entropy stabilization and upon further heating to 900 °C in air, Au re-diffused into the lattice, demonstrating self-healing behavior. This concept has been extended to transition metal alloys, such as CoFeCuNi, exsolved from cubic HEO precursors like $Zr_{0.5}(NiFeCuMnCo)_{0.5}O_x$ under H_2 treatment.[19] These alloys could reversibly diffuse into (oxidized) and out (reduced) of the HEO lattice upon thermal cycling. Importantly, catalysts derived from such exsolution processes showed superior thermal stability and catalytic efficiency in CO_2 hydrogenation, a reaction typically plagued by sintering and deactivation of conventional supported catalysts under high temperature and strong reducing conditions. The socketed architecture of the exsolved alloys, *e.g.*, CoNiCu alloy from $Co_3MnNiCuZnO_x$, provides a strong metal–support interface and enhanced electron transfer, offering a distinct advantage over traditional supported metal catalysts.[43] Preliminary studies have demonstrated the potential of utilizing the dynamic regenerability of HEOs to develop stable and efficient metal catalysts. However, current research primarily focuses on dense, bulk-phase HEO catalysts, where the utilization efficiency of active sites remains low, as many are embedded deep within the bulk structure. To address this limitation, the development of thin-layer and amorphous HEO catalysts has emerged as a promising strategy to maximize the accessibility and utilization of active sites.[20] For example, an ultrasonication-assisted approach could generate HEO particles with much smaller size than the high temperature-involved calcination procedures.[44–46] Nevertheless, studies exploring the dynamic regeneration behavior of amorphous HEOs are still scarce, particularly in comparison to their bulk crystalline counterparts, leaving a critical knowledge gap in understanding their structural evolution and catalytic performance under redox conditions.

In this work, the reversible exsolution–dissolution behavior of HEO catalysts is systematically investigated, focusing on the influence of structural architectures by comparing crystalline and amorphous phases. By employing a suite of complementary characterization techniques, including *in situ* variable-temperature powder X-ray diffraction (PXRD), X-ray photoelectron spectroscopy (XPS), electron microscopy, and *in situ* CO diffuse reflectance infrared Fourier transform spectroscopy (CO-DRIFTS), the structural evolution of both crystalline (c-HEO) and amorphous (a-HEO) phases under redox conditions are elucidated. The results reveal that in a reducing atmosphere, both HEO phases undergo exsolution of metallic species, either as single metals or alloys, which can subsequently re-dissolve into the host lattice upon exposure to oxidizing environments. Notably, compared to their crystalline counterparts, amorphous HEOs exhibit significantly more facile and dynamic exsolution–dissolution behavior, attributed to their higher reducibility and structural disorder. These findings highlight the potential of amorphous HEOs as efficient, self-regenerating catalyst platforms capable of achieving alloy evolution under relatively mild conditions. This work provides fundamental insights into the dynamic regeneration mechanisms of HEOs and underscores the importance of structural architecture design in maximizing active site accessibility, reversibility, and catalytic performance.
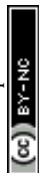
2 Methods

2.1 Synthesis of c-HEO

The dense-phase and highly crystalline HEO (c-HEO) composed of Ni, Mg, Cu, Zn, Co, and O was prepared *via* a combined mechanochemical and calcination procedure.[37] Specifically, each (2 mmol) of MgO, ZnO, CoO, CuO, and NiO (molar ratio $1:1:1:1:1$) was weighed and thoroughly mixed using an agate mortar. To ensure homogeneous mixing, all batches were subsequently ball-milled for at least 2 hours. The resulting powder mixture was then calcined in air at 900 °C for 4 hours (heating rate: 5 °C min^{-1}) to yield the desired bulk-phase HEO.

2.2 Synthesis of a-HEO

The amorphous HEO (a-HEO) with thin layer morphology was synthesized *via* a controlled deposition–precipitation approach in solution. A total of 2 mmol each of $Mg(NO_3)_2\cdot 6H_2O$, $Cu(NO_3)_2\cdot 3H_2O$, $Co(NO_3)_2\cdot 6H_2O$, $Ni(NO_3)_2\cdot 6H_2O$, and $Zn(NO_3)_2\cdot 6H_2O$ were dissolved in 80 mL of deionized water under stirring at room temperature. After 15 minutes, 1.8 g of SBA-15 (Santa Barbara Amorphous-15) was added to the solution and stirred for an additional 30 minutes. Subsequently, 4.4 mL of aqueous ammonia solution (25 wt%) was introduced, and the mixture was continuously stirred for 6 hours. The suspension was then heated to 80 °C to facilitate gradual ammonia evaporation, allowing the pH to decrease to 7. The resulting product was collected by filtration, thoroughly rinsed with deionized water to remove residual ammonium ions, dried at 80 °C under vacuum for 12 hours, and finally calcined in air at 600 °C for 4 hours.

### 2.3 Inductively coupled plasma optical emission spectrometry (ICP-OES)

Inductively coupled plasma-optical emission spectroscopy (ICP-OES) analyses were conducted using an Agilent 5110 ICP-OES system equipped with an Agilent SPS 4 autosampler.

2.4 *In situ* variable-temperature powder X-ray diffraction (PXRD)

In situ variable-temperature powder X-ray diffraction (PXRD) measurements were conducted using the PANalytical Empyrean diffractometer operated at 45 kV and 40 mA. Diffraction patterns were collected over a 2θ range of 20–80° with a step size of 0.02° and a wavelength of $\lambda = 0.1540598$ nm. For the *in situ* measurements, the sample was placed in the instrument and heated stepwise under a 2% H_2 atmosphere, with data collected at every 100 °C/50 °C interval. Upon reaching a designated temperature, the gas environment was switched from hydrogen to air, and data collection continued with further temperature increases to a designated temperature.

2.5 Hydrogen temperature programmed reduction (H$_2$-TPR)

The temperature-programmed reduction (TPR) experiments were measured on a Micromeritics AutoChem II 2920 apparatus. To test, 100 mg of catalyst was loaded into a U-shaped quartz tube and pretreated at 350 °C for 1 h in 5% O_2/He mixture. After pretreatment, the sample was then cooled to 100 °C and then reduced in a flow of 10% H_2 balanced with Ar (30 mL min^{-1}) from 100 to 900 °C
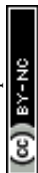
with a ramp rate of 10 °C min^{-1}. The consumption of H$_2$ was monitored using a TCD detector.

2.6 Oxygen temperature programmed oxidation (O$_2$-TPO)

The temperature-programmed oxidation (TPO) experiments were measured on a Micromeritics AutoChem II 2920 apparatus. Each catalyst was reduced *ex situ* at 600 °C in a 5% H$_2$/N$_2$ mixture for 1 hour with a 5 °C min^{-1} ramp rate. Then, 100 mg of catalyst was loaded into a U-shaped quartz tube and pretreated at 350 °C for 1 h in He. After pretreatment, the sample was then cooled to 100 °C and then oxidized in a flow of 5% O$_2$ balanced with He (30 mL min^{-1}) from 100 to 900 °C with a ramp rate of 10 °C min^{-1}. The consumption of O$_2$ was monitored using a TCD detector.

2.7 X-ray photoelectron spectroscopy (XPS)

X-ray photoelectron spectroscopy (XPS) analyses were performed using a Thermo Scientific K-Alpha instrument equipped with a micro-focused, monochromatic Al Kα X-ray source (1486.6 eV). The X-ray beam spot size is adjustable from 30 to 400 μm; for most measurements, a 400 μm spot was used to maximize signal intensity and provide representative surface composition over a large area. The instrument features a hemispherical electron energy analyzer coupled with a 128-channel detection system. The base pressure in the analysis chamber was typically maintained at or below 2×10^{-9} mbar. Spectral deconvolution and quantification were carried out using the CasaXPS software package.

2.8 HAADF-STEM images and EDX element mapping

The high-resolution electron micrographs and energy-dispersive X-ray (EDX) maps were acquired using a Thermo Fisher Scientific Spectra 300 aberration-corrected scanning transmission electron microscope (STEM) operated at 200 keV. The instrument offers a point resolution of 0.08 nm in aberration-corrected mode and is equipped with a SuperX™ detector system comprising four silicon drift detectors for high-throughput X-ray mapping. EDX mapping was conducted using an average beam current of 100 pA, with a resolution of 512×512 pixels and a dwell time of 50 μs per pixel. Each elemental map was generated by summing 10 individual frames. Drift correction and data processing were carried out using Velox software.

2.9 CO diffuse reflectance infrared Fourier transform spectroscopy (DRIFTS)

Carbon monoxide diffuse reflectance infrared Fourier transform spectroscopy (CO-DRIFTS) analysis after calcination was conducted using a Thermo Fisher Nicolet iS50 FTIR spectrometer equipped with a liquid nitrogen-cooled MCT detector. Samples were pretreated in a Harrick Scientific diffuse reflectance cell with temperature control, initially heated to 150 °C under a helium flow for 30 minutes. Subsequently, temperature-programmed reduction under 5% H$_2$/Ar or oxidation under air was performed as required, followed by CO-DRIFTS analysis. After pretreatment, background spectra were recorded at 30 °C. The sample was then exposed to a 1% CO/He mixture (30 mL min^{-1}) for 10 minutes at 30 °C, followed by a 10 minutes purge with He (30 mL min^{-1}) to remove physisorbed CO.
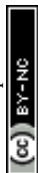
Spectra were collected at 1 minute intervals throughout the adsorption–desorption cycle, with 50 scans per spectrum at a resolution of 0.4 cm^{-1}.

3   Results and discussion

To elucidate the reversible exsolution–dissolution behaviour of HEO in crystalline and amorphous phases, two HEO catalysts possessing rock salt structures are synthesized *via* developed approaches (Fig. 1A). Dense phase and highly crystalline HEO (c-HEO) composed of Ni, Mg, Cu, Zn, Co, and O was prepared *via* a combined mechanochemical and calcination procedure.[37] Specifically, the equimolar ratio mixture of metal oxides was homogenized by ball milling and then calcined at 900 °C in air to obtain the desired bulk-phase HEO (see the Methods section for details). In contrast, amorphous HEO (a-HEO) with thin layer morphology was synthesized *via* a controlled deposition–precipitation approach in solution. Initially, aqueous solutions containing nitrate salts of Ni^{2+}, Mg^{2+}, Cu^{2+}, Zn^{2+}, and Co^{2+} were prepared, and their pH values were precisely adjusted using aqueous ammonia. Subsequently, mesoporous silica (SBA-15) was introduced to facilitate adsorption of the resulting metal cations. The pH of the solution was then gradually lowered from 12 to 7 through controlled evaporation of ammonia, converting the adsorbed metal species into their hydroxide
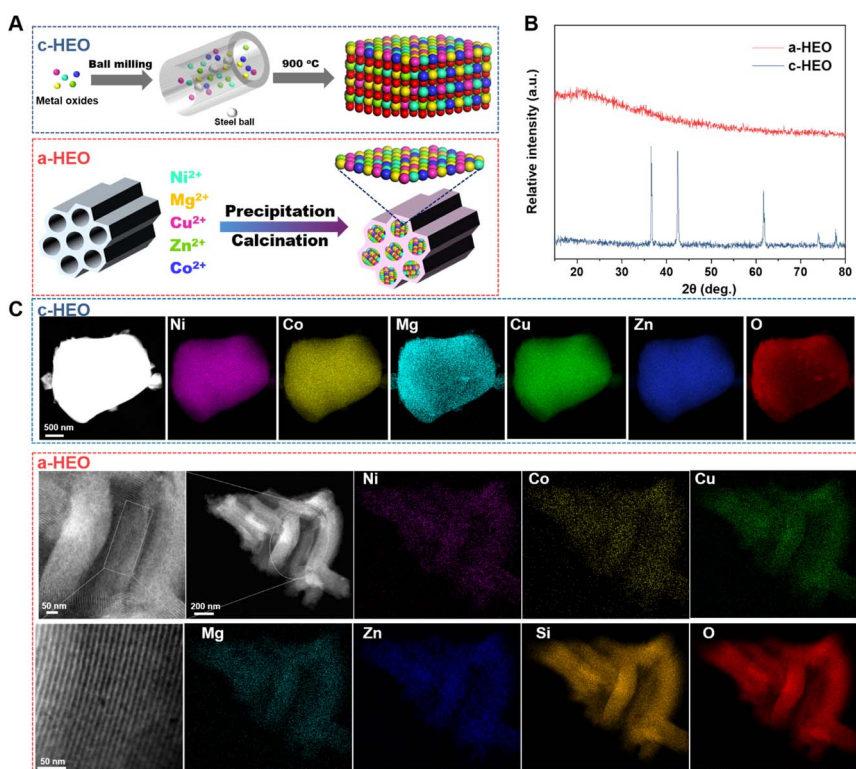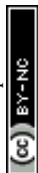

Fig. 1   (A) Synthesis procedure and characterization of c-HEO and a-HEO by (B) XRD; (C) SEM, TEM, and elemental mapping.

counterparts. A subsequent calcination step at 600 °C in an air atmosphere led to the decomposition of metal hydroxide precursors and the formation of a uniform amorphous HEO thin layer on the mesoporous support. The metal cation compositions of c-HEO and a-HEO samples were quantitatively determined by inductively coupled plasma (ICP) analysis. The c-HEO sample contained Ni (20.59 wt%), Mg (7.37 wt%), Cu (21.11 wt%), Zn (20.79 wt%), and Co (18.84 wt%), while the metal contents for the a-HEO sample were: Ni (5.13 wt%), Mg (3.34 wt %), Cu (4.78 wt%), Zn (4.98 wt%), and Co (5.02 wt%).

Powder X-ray diffraction (PXRD) was employed to characterize the crystallo-graphic structures and phase purity of the synthesized HEO samples. For the bulk-phase high-entropy oxide (HEO), the XRD pattern exhibited well-defined diffraction peaks at approximately 36.9°, 42.8°, and 62.2°, indexed to the (111), (200), and (220) crystallographic planes of the rock-salt structure, respectively (Fig. 1B). In contrast, the XRD pattern of the mesoporous silica-supported HEO films predominantly displayed a broad amorphous signal originating from the silica substrate, with no detectable diffraction peaks corresponding to the rock-salt structure. This clearly indicates that the HEO in a-HEO exists as ultrathin amorphous films uniformly deposited on the inner surfaces of the silica support channels without forming larger crystalline particles (Fig. 1B). The morphology and elemental distributions of the synthesized bulk and amorphous HEO were further characterized by electron microscopy. High-angle annular dark-field scanning transmission electron microscopy (HAADF-STEM) imaging clearly revealed that the crystalline high-entropy oxide (c-HEO) exhibited large particle morphology indicative of the bulk phase (Fig. 1C). In contrast, the amorphous high-entropy oxide (a-HEO) maintained the highly ordered mesoporous structure of SBA-15 after HEO deposition, with no apparent formation of nanoparticles or aggregates observed. Additionally, STEM coupled with energy-dispersive X-ray spectroscopy (EDS) elemental mapping confirmed that metal cations (Ni, Mg, Cu, Zn, and Co) were homogeneously distributed across both c-HEO and a-HEO samples, uniformly dispersed without evident segregation or clustering of any specific metallic species (Fig. 1C).

First *in situ* variable-temperature powder X-ray diffraction (PXRD) was per-formed to monitor and compare the exsolution–dissolution behavior of c-HEO and a-HEO. As shown in Fig. 2A, under a programmed temperature increase in a 2% hydrogen (in He) atmosphere, the PXRD patterns of c-HEO remained unchanged up to 500 °C. However, at 600 °C, new diffraction peaks corresponding to metallic species began to emerge. As the temperature increased further to 700 °C, prominent peaks attributed to Cu–Co–Ni alloy were clearly observed, indicating the formation of alloy nanoparticles through an exsolution process. Upon switching the atmosphere from hydrogen to air at 700 °C, these metallic alloy peaks immediately transformed into metal oxide peaks. Raising the temperature further to 850 °C resulted in the disappearance of these oxide peaks (Fig. 2B), indicating that the alloy nanoparticles dissolved back into the bulk oxide phase under oxidative conditions. These observations demonstrate the clear reversible exsolution–dissolution behavior in c-HEO. A similar methodology was applied to study the phenomenon in a-HEO (Fig. 2C). Due to the higher reducible feature of amorphous phases, metallic phases appeared at a significantly lower tempera-ture, observed initially at 350 °C and becoming prominent at 450 °C. Additionally, when the gas atmosphere was switched from hydrogen to air at 450 °C, the
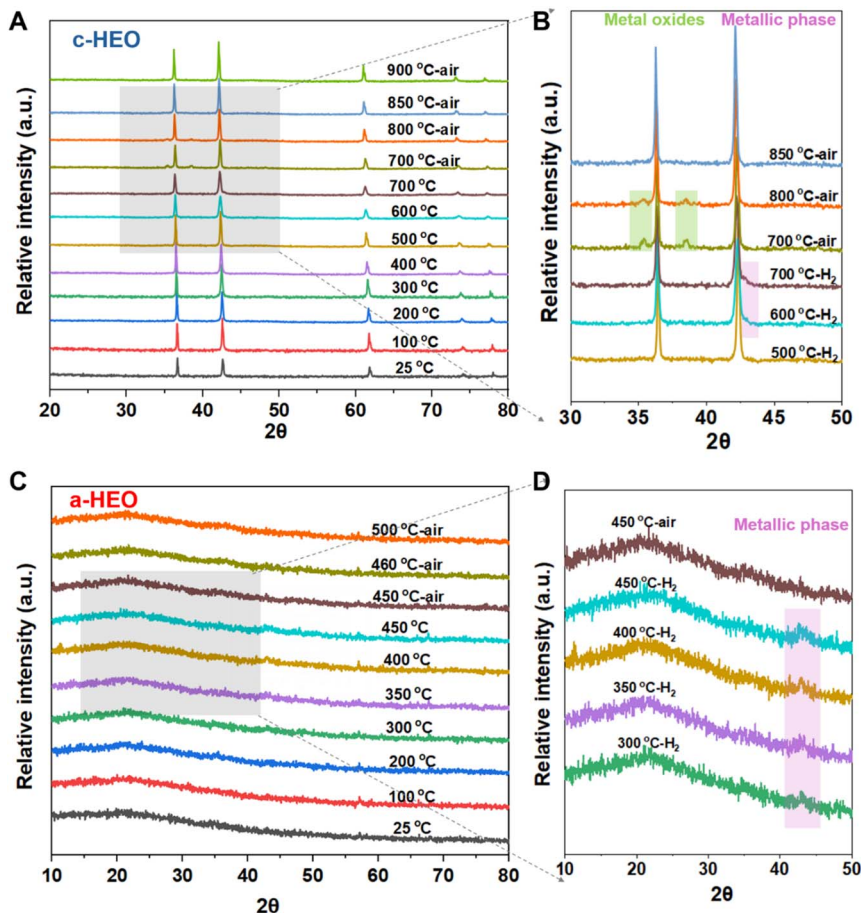
Fig. 2 *In situ* XRD patterns of c-HEO (A and B) and a-HEO (C and D) collected at programmed temperatures under reducing (2% H_2 in He) and oxidative (air) atmospheres.

metallic peaks immediately vanished, confirming rapid dissolution back into the amorphous oxide matrix (Fig. 2D). These findings clearly suggest that a-HEO exhibits more facile exsolution and dissolution processes compared to c-HEO, that is, the reversible self-healing of alloys can be induced under relatively mild conditions.

To further investigate the reducibility of the high-entropy oxides and the influence of crystallinity on the exsolution behavior, hydrogen temperature-programmed reduction (H_2-TPR) was performed on both c-HEO and a-HEO samples. As shown in Fig. 3A, the TPR profile of a-HEO exhibits a prominent hydrogen consumption peak centered around 250 °C, followed by a broad feature around 400–700 °C. In contrast, the c-HEO sample shows a shifted initial reduction peak at ~325 °C, a smaller intermediate peak at ~550 °C, and a broader reduction envelope from 700–900 °C. The low-temperature peak at ~250 °C in a-HEO is attributed to the facile reduction of Cu species ($Cu^{2+} \rightarrow Cu^0$), which is known to occur at relatively low temperatures, particularly when copper is
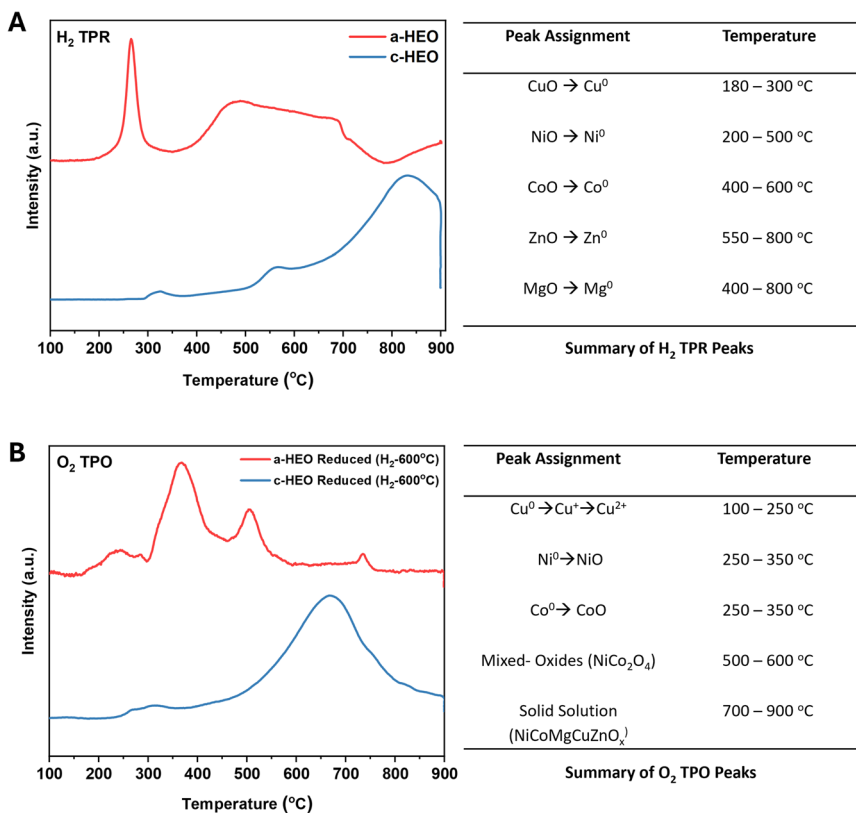
A

**H₂ TPR** — a-HEO / c-HEO

Peak Assignment	Temperature
CuO → Cu⁰	180 – 300 °C
NiO → Ni⁰	200 – 500 °C
CoO → Co⁰	400 – 600 °C
ZnO → Zn⁰	550 – 800 °C
MgO → Mg⁰	400 – 800 °C
Summary of H₂ TPR Peaks	

B

O₂ TPO — a-HEO Reduced (H₂-600°C) / c-HEO Reduced (H₂-600°C)

Peak Assignment	Temperature
Cu⁰ → Cu⁺ → Cu²⁺	100 – 250 °C
Ni⁰ → NiO	250 – 350 °C
Co⁰ → CoO	250 – 350 °C
Mixed- Oxides (NiCo₂O₄)	500 – 600 °C
Solid Solution (NiCoMgCuZnOₓ)	700 – 900 °C
Summary of O₂ TPO Peaks	

Fig. 3 (A) H₂ TPR analysis of a-HEO and c-HEO with summary of H₂ TPR peaks; (B) O₂ TPO analysis of a-HEO reduced at 600 °C in H₂ and c-HEO reduced at 600 °C with summary of O₂ TPO peaks.

atomically dispersed or poorly coordinated within an amorphous matrix.[47] The shift of this reduction feature to ~325 °C in c-HEO implies that Cu is more strongly bound or structurally stabilized within the crystalline oxide lattice, likely requiring higher activation energy for reduction. The broader reduction peak from 400–700 °C observed in a-HEO is consistent with the stepwise reduction of Ni^{2+} and Co^{2+} species and the progressive formation of Cu–Ni–Co alloy nanoparticles, which is also supported by *in situ* PXRD data showing alloy emergence at 450–600 °C.[48] Conversely, c-HEO displays a more segmented reduction process, with a discernible intermediate peak at 550 °C attributed to isolated Ni^{2+} or Co^{2+} species requiring higher temperatures for reduction, consistent with their known reducibility in crystalline mixed oxides.[49] The delayed, high-temperature reduction feature from 700–900 °C suggests further reduction of bulk-stabilized metal ions and possibly partial reduction of Zn^{2+} or Mg^{2+} species, or more strongly coordinated Co/Ni species, requiring elevated temperatures to initiate oxygen abstraction and alloy formation.[50]

O_2 temperature-programmed oxidation (O_2-TPO) was performed following the H_2-TPR experiments to reinforce the redox dynamics and probe the oxidative reversibility of the exsolved metallic phases. As shown in Fig. 3B, the a-HEO
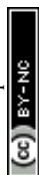
sample exhibits four distinct O_2 consumption features: a weak low-temperature peak at ~250 °C, a dominant peak centered at ~350 °C, a medium-intensity peak at ~500 °C, and a minor broad feature around ~750 °C. The pronounced 350 °C oxidation peak in a-HEO corresponds to the rapid re-oxidation of exsolved Cu–Ni–Co alloys, which were previously formed at lower temperatures under H_2 atmosphere.[51] The preceding ~250 °C shoulder likely reflects early-stage $Cu^0 \rightarrow Cu^{2+}$ oxidation, occurring as discrete or atomically dispersed Cu sites oxidize.[52] The intermediate ~500 °C peak in a-HEO is attributed to reformation of mixed metal oxides or spinel-like phases (e.g., $NiCo_2O_4$), consistent with the broader multi-step reduction profile seen in H_2-TPR.[53] In contrast, the c-HEO sample exhibits delayed and broader oxidation behavior, with the majority of O_2 uptake occurring only after 500 °C. The presence of high-temperature oxidation from ~700–800 °C may also point toward solid-solution reconstruction, where entropy-stabilized configurations are gradually re-established.[54] Together, the H_2-TPR and O_2-TPO analyses reveal distinct redox behaviors between the amorphous and crystalline high-entropy oxides, directly reflecting the structural features established earlier in the study. The a-HEO sample exhibits enhanced reducibility and oxidative reversibility, with sharp H_2 consumption peaks at lower temperatures and well-resolved O_2 uptake features at moderate temperatures, which are signatures of facile alloy exsolution and rapid reintegration of metal species into the oxide matrix.

To further investigate the reversible exsolution–dissolution behaviour, X-ray photoelectron spectroscopy (XPS) analysis was conducted for c-HEO and a-HEO samples (Fig. 4). All elemental spectra were calibrated using the C–C peak at 284.8 eV in the C 1s spectrum as a reference. In the case of c-HEO, XPS spectra were compared among the pristine, reduced sample (annealed at 600 °C under a 5% H_2/Ar atmosphere), and the re-oxidized sample (treated at 900 °C in an air atmosphere). The Zn $2p_{3/2}$ (1021.8 eV) and Mg 1s (1303.8 eV) spectra reveal that
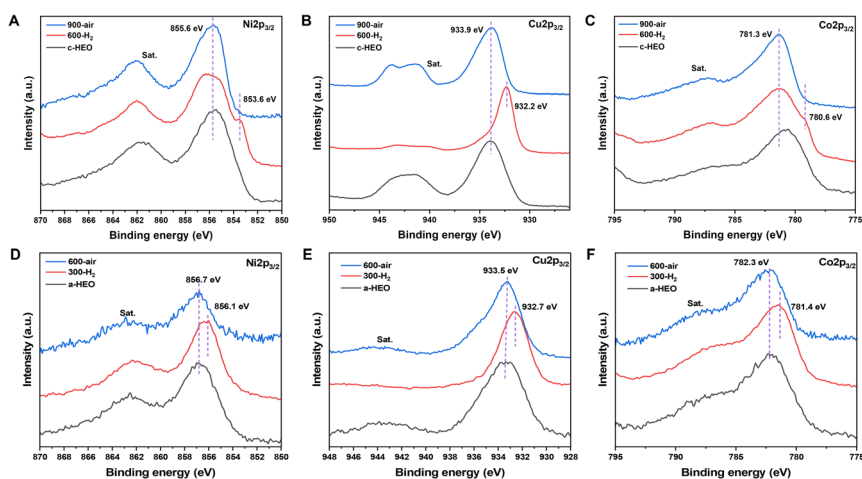

Fig. 4 XPS spectra for pristine, reduced (5% H_2/Ar at 600 °C), and re-oxidized (air at 900 °C) c-HEO (A: Ni 2p region; B: Cu 2p region; C: Co 2p region), and pristine, reduced (5% H_2/Ar at 300 °C), and re-oxidized (air at 600 °C) a-HEO (D: Ni 2p region; E: Cu 2p region; F: Co 2p region) samples.

Paper

both Zn and Mg consistently exist in the +2 oxidation state. In contrast, the Ni 2p (Fig. 4A), Cu 2p (Fig. 4B), and Co 2p (Fig. 4C) spectra exhibited significant changes after the reduction and subsequent re-oxidation treatments. Upon reduction, characteristic peaks corresponding to the metallic states emerged at 853.6 eV (Ni $2p_{3/2}$), 932.2 eV (Cu $2p_{3/2}$), and 780.6 eV (Co $2p_{3/2}$), while coexisting with the peaks attributed to oxidized species further confirm the partial exsolution of the NiCuCo alloy from the HEO matrix upon reduction.[19,24,35] Following re-oxidation, the metallic peaks disappeared, and the spectra reverted to oxidized-state profiles, suggesting that the exsolved NiCuCo alloy dissolved into the HEO matrix. These observations are consistent with the structural changes confirmed by *in situ* XRD patterns. A similar reversible exsolution–dissolution behavior was observed for a-HEO, but under significantly milder conditions (Fig. 4D–F). After reduction at 300 °C, XPS spectra displayed distinct metallic peaks for Cu, Co, and Ni, confirming the exsolution of these species from the amorphous HEO matrix. Following air oxidation at 600 °C, the metallic XPS peaks completely disappeared, and the spectra reverted to the fully oxidized state. This confirms that the exsolved NiCuCo alloy species were fully re-dissolved into the amorphous HEO matrix, completing the reversible cycle.
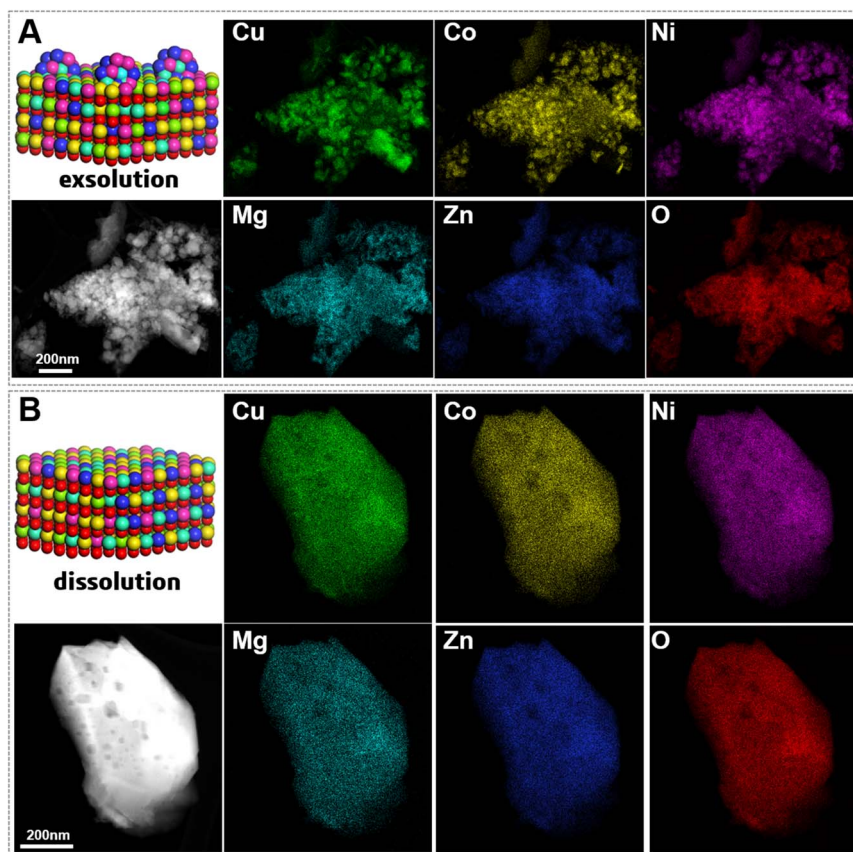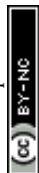

Fig. 5 Microscopy of treated samples of c-HEO after reduction under 5% H_2 at 600 °C (A) and subsequent oxidation under air at 900 °C (B).

Furthermore, the structure evolution and elemental distribution variation of c-HEO upon thermal treatment under diverse gas atmospheres are probed by electron microscopy to provide additional insights into the exsolution–dissolution process. As illustrated in Fig. 5A, under reducing conditions, metallic copper, cobalt, and portions of nickel exsolved from the HEO matrix, forming nanoparticles that may consist of pure metals or alloys. During the oxidation process, these exsolved metal phases dissolved back into the HEO matrix, effectively reconstructing the original structure (Fig. 5B), and the darker regions observed on the surface indicated sites where metal exsolution had previously occurred. In the case of a-HEO, electron microscopy revealed that all five metal elements remained well dispersed in both the reduced and re-oxidized samples, with no detectable exsolved metal phase, likely due to the extremely small size of the nanoparticles, which may reside within the pore channels of SBA15 and fall below the resolution limit of the instrument (Fig. 6). This comprehensive analysis demonstrates the distinct reversible exsolution–dissolution behavior in both c-HEO and a-HEO, with the amorphous phase exhibiting a more rapid and facile reversible regeneration process.

Based on the understanding in the exsolution–dissolution variation of HEO with different architectures, their gas adsorption behavior was further studied
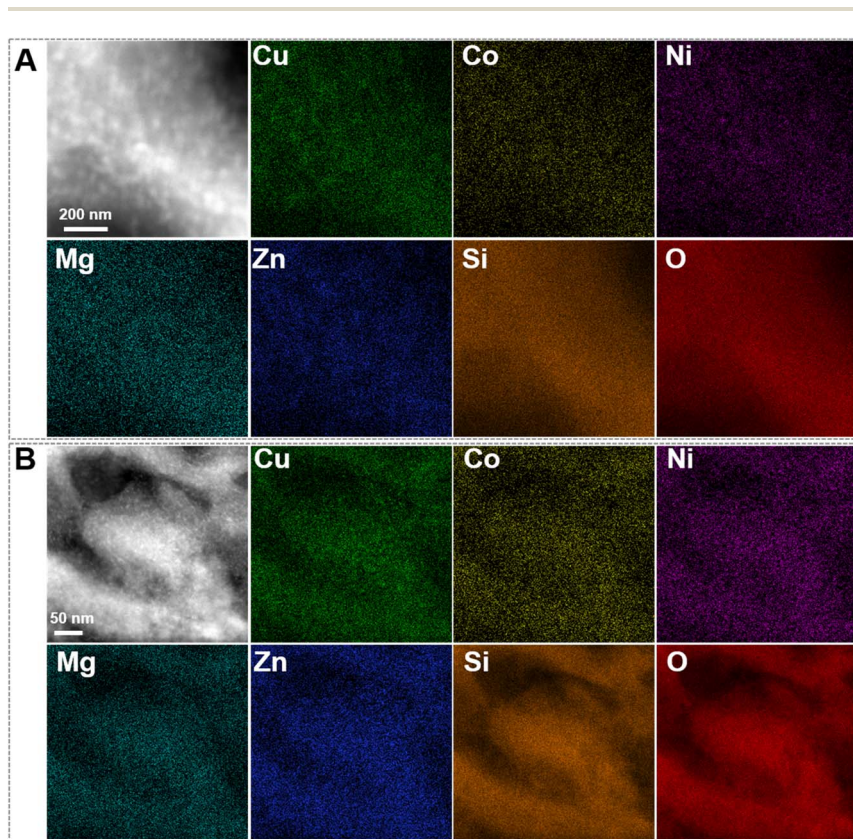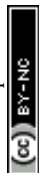

Fig. 6 Microscopy of treated samples of a-HEO after reduction under 5% H_2 at 300 °C (A) and subsequent oxidation under air at 350 °C (B).
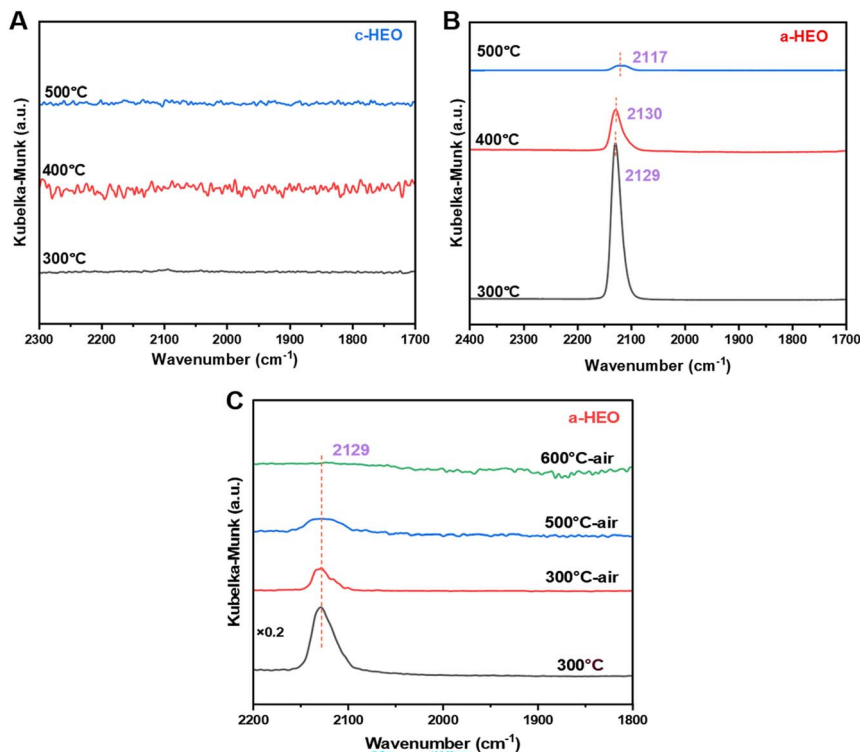
Fig. 7   CO-DRIFTS results of c-HEO (A) and a-HEO (B) at different reduction temperatures under 5% H_2/Ar atmosphere and a-HEO (C) at different oxidation temperatures under air atmosphere.

using CO as probe molecules (Fig. 7). For the c-HEO sample, the CO diffuse reflectance infrared Fourier transform spectroscopy (DRIFTS) results indicate that after being subjected to different reduction temperatures (up to 500 °C under 5% H_2/Ar atmosphere), they do not exhibit any significant CO adsorption peaks (Fig. 7A). This could be attributed to the low specific surface area of the bulk HEO (around 5 m^2 g^{-1}),[35] which limits the number of accessible metal sites for CO binding. In addition, the dark coloration of the c-HEO sample after reduction further attenuates the IR signal, resulting in a decreased signal-to-noise ratio and weakened spectra. In contrast, the a-HEO uniformly dispersed in the mesoporous material exhibits a distinct CO adsorption peak (2129 cm^{-1}) after reduction at 300 °C, which belonged to adsorbed CO molecules on metallic Cu species.[55] Notably, a slight redshift was observed by further increasing the reduction temperature to 500 °C, which can be attributed to local electronic structure changes induced by the gradual exsolution of the NiCoCu alloy.[56] However, with increasing reduction temperature, the catalyst exhibits a progressively darker color, which in turn attenuates the signal intensity detected by the instrument. Consequently, the resulting spectra appear increasingly weakened and broadened.[57] Further examination of the redox process revealed that after air oxidation at elevated temperatures, the CO adsorption peak at 2129 cm^{-1} gradually decreased in intensity. Importantly, after oxidation at 600 °C, the CO peak
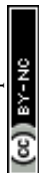
completely disappeared, indicating that the exsolved metallic species were fully re-oxidized and reincorporated into the a-HEO matrix (Fig. 7C). This observation is consistent with the XPS results, which also confirm the complete oxidation of the exsolved metal alloy at 600 °C.

4 Conclusions

In summary, the reversible exsolution–dissolution behavior of high-entropy oxides (HEOs) with distinct structural architectures—crystalline (c-HEO) and amorphous (a-HEO)—were systematically investigated to elucidate their dynamic structural evolution and catalytic regeneration potential under redox conditions. Using a comprehensive suite of *in situ* and *ex situ* characterization techniques, including variable-temperature PXRD, H_2-TPR, O_2-TPO, XPS, electron microscopy, and CO-DRIFTS, we revealed that both HEO phases exhibit clear reversible exsolution of metallic species or alloys in reducing atmospheres, followed by reincorporation into the oxide matrix upon re-oxidation. The amorphous HEOs exhibited significantly lower reduction temperatures and more rapid reversibility, enabling self-healing of active metal species under milder conditions. This enhanced redox responsiveness is attributed to the structural disorder and higher reducibility of the amorphous matrix, which promotes efficient diffusion and reversible reconstruction of metal species. These findings provide fundamental insights into the architecture-dependent dynamics of HEOs and highlight the potential of amorphous HEOs as a promising platform for the design of regenerable and durable catalysts. By maximizing active site accessibility and enabling low-temperature regeneration, this study opens new avenues for the development of advanced catalytic systems that leverage the intrinsic flexibility of high-entropy materials.

Author contributions

S. Dai conceived the original idea. Q. Wang and H. Yu conducted the catalyst synthesis and characterization. K. Siniard conducted the characterization. Z. Yang revised the manuscript. All authors contributed to discussions on experimental procedures, data analysis, and manuscript organization.
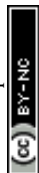
Conflicts of interest

There are no conflicts to declare.

Data availability

All the data is presented in the manuscript.

Acknowledgements

Notes and references

1 Y. Sun and S. Dai, *Sci. Adv.*, 2021, **7**, eabg1600.

2 Y. Zhai, X. Ren, B. Wang and S. Liu, *Adv. Funct. Mater.*, 2022, **32**, 2207536.

3 Y. Xin, S. Li, Y. Qian, W. Zhu, H. Yuan, P. Jiang, R. Guo and L. Wang, *ACS Catal.*, 2020, **10**, 11280–11306.

4 C. Zhan, L. Bu, H. Sun, X. Huang, Z. Zhu, T. Yang, H. Ma, L. Li, Y. Wang, H. Geng, W. Wang, H. Zhu, C.-W. Pao, Q. Shao, Z. Yang, W. Liu, Z. Xie and X. Huang, *Angew. Chem., Int. Ed.*, 2023, **62**, e202213783.

5 H. Wu, Q. Lu, Y. Li, M. Zhao, J. Wang, Y. Li, J. Zhang, X. Zheng, X. Han, N. Zhao, J. Li, Y. Liu, Y. Deng and W. Hu, *J. Am. Chem. Soc.*, 2023, **145**, 1924–1935, DOI: 10.1021/jacs.2c12295.

6 S. Akrami, Y. Murakami, M. Watanabe, T. Ishihara, M. Arita, M. Fuji and K. Edalati, *Appl. Catal., B*, 2022, **303**, 120896.

7 T. Wang, J. Fan, C.-L. Do-Thanh, X. Suo, Z. Yang, H. Chen, Y. Yuan, H. Lyu, S. Yang and S. Dai, *Angew. Chem., Int. Ed.*, 2021, **60**, 9953–9958.

8 M. Zhang, K. Luo, Y. Fan, X. Lu, J. Ye, N. Lu, J. Dong, Q. Niu, J. Zhang and P. Zhang, *Chem. Eng. J.*, 2024, **493**, 152758.

9 S. Hou, L. Su, S. Wang, Y. Cui, J. Cao, H. Min, J. Bao, Y. Shen, Q. Zhang and Z. Sun, *Adv. Funct. Mater.*, 2024, **34**, 2307923.

10 T. Jin, X. Sang, R. R. Unocic, R. T. Kinch, X. Liu, J. Hu, H. Liu and S. Dai, *Adv. Mater.*, 2018, **30**, 1707512.

11 Y. Wang and Y. Wang, *Nano Energy*, 2022, **104**, 107958.

12 S. S. Araya, F. Zhou, V. Liso, S. L. Sahlin, J. R. Vang, S. Thomas, X. Gao, C. Jeppesen and S. K. Kær, *Int. J. Hydrogen Energy*, 2016, **41**, 21310–21344.

13 A. Amiri and R. Shahbazian-Yassar, *J. Mater. Chem. A*, 2021, **9**, 782–823.

14 Y. Leng, Z. Zhang, H. Chen, S. Du, J. Liu, S. Nie, Y. Dong, P. Zhang and S. Dai, *Chem. Commun.*, 2021, **57**, 3676–3679.

15 B. Liang, Y. Ai, Y. Wang, C. Liu, S. Ouyang and M. Liu, *Materials*, 2020, **13**, 5798.

16 Y. Wang, J. Mi and Z.-S. Wu, *Chem Catal.*, 2022, **2**, 1624–1656.

17 Y. Ma, Y. Ma, Q. Wang, S. Schweidler, M. Botros, T. Fu, H. Hahn, T. Brezesinski and B. Breitung, *Energy Environ. Sci.*, 2021, **14**, 2883–2905.

18 B. Jiang, C. A. Bridges, R. R. Unocic, K. C. Pitike, V. R. Cooper, Y. Zhang, D. Y. Lin and K. Page, *J. Am. Chem. Soc.*, 2021, **143**, 4193–4204.

19 S. Hou, X. Ma, Y. Shu, J. Bao, Q. Zhang, M. Chen, P. Zhang and S. Dai, *Nat. Commun.*, 2021, **12**, 5917.

20 J. Liang, J. Liu, H. Wang, Z. Li, G. Cao, Z. Zeng, S. Liu, Y. Guo, M. Zeng and L. Fu, *J. Am. Chem. Soc.*, 2024, **146**, 7118–7123.

21 M. Zhang, Y. Gao, C. Xie, X. Duan, X. Lu, K. Luo, J. Ye, X. Wang, X. Gao and Q. Niu, *Nat. Commun.*, 2024, **15**, 8306.

22 C. M. Rost, E. Sachet, T. Borman, A. Moballegh, E. C. Dickey, D. Hou, J. L. Jones, S. Curtarolo and J.-P. Maria, *Nat. Commun.*, 2015, **6**, 8485.

23 H. Chen, J. Fu, P. Zhang, H. Peng, C. W. Abney, K. Jie, X. Liu, M. Chi and S. Dai, *J. Mater. Chem. A*, 2018, **6**, 11129–11133.

24 M. Zhang, J. Ye, Y. Gao, X. Duan, J. Zhao, S. Zhang, X. Lu, K. Luo, Q. Wang, Q. Niu, P. Zhang and S. Dai, *ACS Nano*, 2024, **18**, 1449–1463.
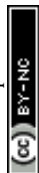
25 Y. Sun, T. Wu, Z. Bao, J. Moon, Z. Huang, Z. Chen, H. Chen, M. Li, Z. Yang and M. Chi, *ACS Cent. Sci.*, 2022, **8**, 1081–1090.

26 T. Wang, H. Chen, Z. Yang, J. Liang and S. Dai, *J. Am. Chem. Soc.*, 2020, **142**, 4550–4554.

27 M. Zhang, X. Zhou, K. Luo, Y. Fan, C. He, Q. Niu, J. Zhang, P. Zhang and S. Dai, *J. Mater. Chem. A*, 2025, **13**, 1287–1301.

28 M. Zhang, X. Lu, K. Luo, J. Ye, J. l. Dong, N. Lu, X. Wang, Q. Niu, P. Zhang and S. Dai, *Appl. Catal., B*, 2024, **349**, 123845.

29 M. Zhang, X. Duan, Y. Gao, S. Zhang, X. Lu, K. Luo, J. Ye, X. Wang, Q. Niu and P. Zhang, *ACS Appl. Mater. Interfaces*, 2023, **15**, 45774–45789.

30 F. Okejiri, Z. Zhang, J. Liu, M. Liu, S. Yang and S. Dai, *ChemSusChem*, 2020, **13**, 111–115.

31 C. Deng, R. Liu, P. Wu, T. Wang, S. Xi, D. Tao, Q. He, Y. Chao, W. Zhu and S. Dai, *Small*, 2024, **20**, 2406685.

32 D. Feng, Y. Dong, L. Zhang, X. Ge, W. Zhang, S. Dai and Z.-A. Qiao, *Angew. Chem., Int. Ed.*, 2020, **59**, 19503–19509.

33 C. Deng, P. Wu, L. Zhu, J. He, D. Tao, L. Lu, M. He, M. Hua, H. Li and W. Zhu, *Appl. Mater. Today*, 2020, **20**, 100680.

34 Z. Zhang, S. Yang, X. Hu, H. Xu, H. Peng, M. Liu, B. P. Thapaliya, K. Jie, J. Zhao, J. Liu, H. Chen, Y. Leng, X. Lu, J. Fu, P. Zhang and S. Dai, *Chem. Mater.*, 2019, **31**, 5529–5536.

35 H. Chen, K. Jie, C. J. Jafta, Z. Yang, S. Yao, M. Liu, Z. Zhang, J. Liu, M. Chi, J. Fu and S. Dai, *Appl. Catal., B*, 2020, **276**, 119155.

36 M. Fracchia, P. Ghigna, T. Pozzi, U. Anselmi Tamburini, V. Colombo, L. Braglia and P. Torelli, *J. Phys. Chem. Lett.*, 2020, **11**, 3589–3593.

37 H. Chen, W. Lin, Z. Zhang, K. Jie, D. R. Mullins, X. Sang, S.-Z. Yang, C. J. Jafta, C. A. Bridges, X. Hu, R. R. Unocic, J. Fu, P. Zhang and S. Dai, *ACS Mater. Lett.*, 2019, **1**, 83–88.

38 D. Chen, S. Nie, L. Wu, X. Zheng, S. Du, X. Duan, Q. Niu, P. Zhang and S. Dai, *Chem. Mater.*, 2022, **34**, 1746–1755.

39 H. Xu, Z. Zhang, J. Liu, C. L. Do-Thanh, H. Chen, S. Xu, Q. Lin, Y. Jiao, J. Wang, Y. Wang, Y. Chen and S. Dai, *Nat. Commun.*, 2020, **11**, 3908.

40 Y. Sun and S. Dai, *Nat. Synth.*, 2024, **3**, 1457–1470.

41 A. López-García, A. J. Carrillo, C. E. Jiménez, R. S. Anzorena, R. Garcia-Diez, V. Pérez-Dieste, I. J. Villar-Garcia, A. B. Hungría, M. Bär and J. M. Serra, *J. Mater. Chem. A*, 2024, **12**, 22609–22626.

42 H. Chen, Y. Sun, S. Yang, H. Wang, W. Dmowski, T. Egami and S. Dai, *Chem. Commun.*, 2020, **56**, 15056–15059.

43 J. Zhao, J. Bao, S. Yang, Q. Niu, R. Xie, Q. Zhang, M. Chen, P. Zhang and S. Dai, *ACS Catal.*, 2021, **11**, 12247–12257.

44 F. Okejiri, J. Fan, Z. Huang, K. M. Siniard, M. Chi, F. Polo-Garzon, Z. Yang and S. Dai, *iScience*, 2022, **25**, 104214.

45 M. Li, K. M. Siniard, D. M. Driscoll, A. S. Ivanov, X. Lu, H. Chen, J. Zhang, F. Polo-Garzon, Z. Yang and S. Dai, *J. Catal.*, 2024, **437**, 115645.

46 K. M. Siniard, M. Li, Y. Cai, J. Zhang, F. Polo-Garzon, D. M. Driscoll, A. S. Ivanov, X. Lu, H. Chen and Y. Li, *ACS Catal.*, 2024, **14**, 14807–14818.

47 J. Zhao, J. Bao, S. Yang, Q. Niu, R. Xie, Q. Zhang, M. Chen, P. Zhang and S. Dai, *ACS Catal.*, 2021, **11**, 12247–12257.
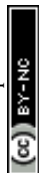
48 H. J. Gallon, X. Tu, M. V. Twigg and J. C. Whitehead, *Appl. Catal., B*, 2011, **106**, 616–620.

49 M. Liang, W. Kang and K. Xie, *J. Nat. Gas Chem.*, 2009, **18**, 110–113.

50 K. Meng, Y. Qi, L. Wen, F. Zheyong, F. Jinhua, X. Zheng and T. D. Wheelock, *Chin. J. Catal.*, 2012, **33**, 1508–1516.

51 Y. Unutulmazsoy, R. Merkle, D. Fischer, J. Mannhart and J. Maier, *Phys. Chem. Chem. Phys.*, 2017, **19**, 9045–9052.

52 B. Chattopadhyay and G. Wood, *Oxid. Met.*, 1970, **2**, 373–399.

53 Y. Law, T. Dintzer and S. Zafeiratos, *Appl. Surf. Sci.*, 2011, **258**, 1480–1487.

54 N. K. Adomako, J. H. Kim and Y. T. Hyun, *J. Therm. Anal. Calorim.*, 2018, **133**, 13–26.

55 J. Greeley, A. Gokhale, J. Kreuser, J. Dumesic, H. Topsøe, N.-Y. Topsøe and M. Mavrikakis, *J. Catal.*, 2003, **213**, 63–72.

56 M. L. Smith, N. Kumar and J. J. Spivey, *J. Phys. Chem. C*, 2012, **116**, 7931–7939.

57 P. Naliwajko, T. Peppel and J. Strunk, *React. Kinet., Mech. Catal.*, 2022, **135**, 2291–2305.